THE JOURNAL OF PHYSICAL CHEMISTRY C

Article

pubs.acs.org/JPCC

Mechanical Response of Aluminosilicate Nanotubes under Compression

Rafael I. González,*[†,§] José Rogan,[†,§] Eduardo M. Bringa,[‡] and Juan Alejandro Valdivia*[†,§]

[†]Departamento de Física, Facultad de Ciencias, Universidad de Chile, Casilla 653, Santiago, Chile 7800024

[‡]CONICET-Argentina. Facultad de Ciencias Exactas y Naturales, Universidad Nacional de Cuyo, Mendoza 5500, Argentina

[§]Centro para el Desarrollo de la Nanociencia y la Nanotecnología, CEDENNA, Avda. Ecuador 3493, Santiago, Chile 9170124

Supporting Information

ABSTRACT: The mechanical response of aluminosilicate nanotubes (imogolite) under compression is investigated by means of classical molecular dynamics simulations using the CLAYFF potential. Using the uncompressed length L_0, when there is no strain, to describe each nanotube, we have found that imogolite tends to coil for $L_0 > 15$ nm to prevent the failure of the nanotube. The simulation also shows that the nanotubes do not break under stress for $L_0 \geq 100$ nm. Hence, the imogolite is a very flexible nanotube, which has been observed with lengths up to 500 nm. Finally, we can report a Young modulus of the order of 200 GPa, which is relatively independent of L_0.

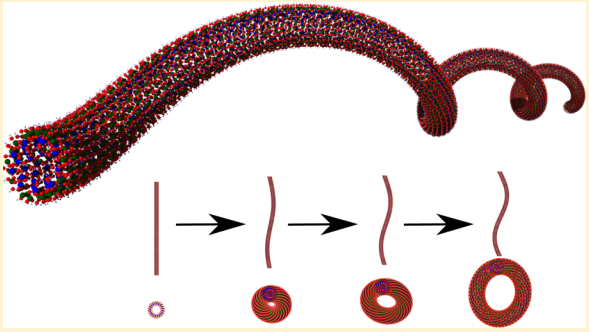

INTRODUCTION

Since the discovery by Iijima[1] of carbon nanotubes (C-NTs), and their inorganic counterpart by Tenne et al.,[2] (inorganic concentric polyhedral and cylindrical structures of tungsten disulfide), cylindrical nanostructures have been intensively investigated by experimentalists and theorists. These hollow cylinders are very attractive because of their fascinating properties and their practical uses. C-NTs, and several inorganic ones, are fabricated by electric arc discharge, laser ablation, or chemical vapor deposition processes, while inorganic oxide NTs, like the aluminosilicate NT, also known as imogolite, which is our present focus of attention, are created mainly by low-temperature liquid phase chemical processes.[3]

In the past few years there has been a growing interest in the study of imogolite NTs because of their many interesting properties. First, it is an inorganic aluminosilicate NT that forms naturally in weathered volcanic ashes,[4] but that can also be synthesized in the laboratory with nearly monodisperse diameters.[5] Imogolite has been suggested as a water filter, because of its arsenic retention capacity.[6,7] Similarly, it could be used to encapsulate drugs[8] because it would allow their sustained release in the body.[8] Other proposals include support for polymers or catalyst,[9−13] use as molecular sieves[14−16] and gas absorbers,[17,18] or part of nanowires and organic−inorganic nanohybrides.[19−27]

It is an insulator[19,28] with monodisperse diameters independent of the diverse synthesis procedures.[29−33] This property is different from other traditional NTs, such as carbon-NTs, which form from the graphitic sheet with a bending energy that decreases monotonically as the NT diameter increases, thus precluding the possibility of tuning the NT diameter. From the theoretical point of view, the monodisperse behavior of imogolite is associated with the fact that the strain energy presents a minimum as a function of its diameter.[28,34−39]

The single walled imogolite has a chemical composition, ordered from the outside of the NT inward, is $[(OH)_3Al_2O_3SiOH]_{2N_\theta}$, that repeats N_θ times in the angular direction and N_z times in the longitudinal direction, as illustrated in Figure 1. This structure, of basic relevance to the study of imogolite, was put forward in 1972 by Cradwick et al.[40] In Figure 1 we highlight that the aluminum atoms forms an

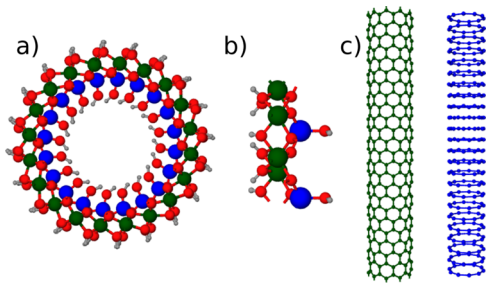

Figure 1. (a) Imogolite structure from an axial point of view. (b) Lateral view of the basic imogolite unit $[(OH)_3Al_2O_3SiOH]_2$, ordered from left to right. (c) Hexagonal array of the aluminum atoms and the ring array for silicon atoms. In both cases, we deleted the rest of atoms to ease visualization. Key: H, light gray; O, red; Si, blue; and Al, green.

Received: May 5, 2016
Revised: June 9, 2016
Published: June 17, 2016

DOI: 10.1021/acs.jpcc.6b04564
J. Phys. Chem. C 2016, 120, 14428−14434

hexagonal array while the inner silicon atoms form concentric rings along the NT axis.

The length of the imogolite NTs can vary from 20 to hundreds of nanometers,[41,42] but it can lose its tubular shape for temperatures above 770 K.[43] Besides its thermal properties, which have been analyzed in a number of manuscripts,[34,35,43] there is little work about its mechanical properties. Its Young modulus has been reported by Guimaraes et al. using the TB-DFT method to be 175−479 GPa, and close to 320−350 GPa has been reported for Ge−imogolite.[38] On the other hand, Teobaldi et al.[44] reported a Young modulus of between 122 and 168 GPa using DFT (range due the definition of imogolite volume). Finally, a value near 340 GPa has been published by Liou et al.[45,46] using a continuum model. As far as we know there is no experimental data available about these mechanical properties of imogolite at the nanoscale.

Therefore, in this manuscript, we analyze the mechanical response of Imogolite under compression. This paper is organized as follows: after this Introduction we describe the method we used in the section Method. Next the results obtained are given in the Results, and the paper is closed with a summary and the drawing of conclusions.

METHODS

The main tool we use is classical molecular dynamics (MD) simulations. These MD simulations, as well as the structural relaxations, were carried out using the large-scale atomic/molecular massively parallel simulator (LAMMPS) code[47] accelerated with the GPU package.[48−50] For the atomic interactions the CLAYFF potential[51] is used, since it has been proven to be adequate to model aluminosilicate (imogolite) NTs.[34−36,52−55]

The CLAYFF potential, developed by Cygan et al., incorporates a Coulomb potential and a van der Waals interaction between all atoms, and an harmonic potential only for the O−H group stretching. Analytically it is given by

$$E = \frac{e^2}{4\pi\epsilon_0}\sum_{i\neq j}\frac{q_i q_j}{r_{ij}} + \sum_{i\neq j}\epsilon_{ij}\left[\left(\frac{R_{0,ij}}{r_{ij}}\right)^{12} - 2\left(\frac{R_{0,ij}}{r_{ij}}\right)^{6}\right] + k_{ij}(r_{ij} - r_0)^2 \quad (1)$$

where the q_i are the partial charges, obtained by means of quantum mechanical calculations, e is the electron charge, and ϵ_0 is the vacuum dielectric permittivity. The second summation corresponds to the van der Waals contribution, where $R_{0,ij}$ and ϵ_{ij} are empirical parameters derived by fitting to bulk structural and physical properties, and r_{ij} represents the distances between atoms i and j. The last term in eq 1 describes the O−H bond stretch energy by means of a simple harmonic interaction, where the k_{ij} values are the stretching constants and r_0 is the equilibrium O−H distance. All these parameters are given in Table 1. Here we do not incorporate charge transfer and/or redistribution to avoid unphysical results, as suggested by Cygan et al.[51]

The Coulomb forces are long ranged, and thus converge slowly as a function of the size of the simulation box, requiring special techniques to handle them and to evaluate their contribution, since the size of the simulation box is a crucial issue. We simulate an isolated NT (only periodic along the z axis) with a simulation box of 200 × 200 Å^2 along the normal plane to the NT (xy plane). The long-range interactions are handled by means of an Ewald sum[56] that is quite efficient to account for the vacuum that is included. Also, it is important to mention that for the graphics and postprocessing of the results we use the Open Visualization Tool code OVITO.[57,58]

Table 1. CLAYFF Parameters Taken from Cygan et al.'s[51] Work[a]

Nonbond Parameters			
species	charge (e)	ϵ (eV)	R_0 (Å)
hydroxyl H	0.425	0	0
hydroxyl O	−0.950	6.7×10^{-3}	3.5532
bridging O	−1.050	6.7×10^{-3}	3.5532
octahedral Al	1.575	5.7×10^{-8}	4.7943
tetrahedral Si	2.100	8.0×10^{-8}	3.7064
Bond Parameters			
species i	species j	k (eV/Å^2)	r_0 (Å)
hydroxyl O	hydroxyl H	24.03	1.0

[a]The "bond parameters" parameterize the bond stretching.

In this work we are interested in the mechanical response of imogolite under compression, and its dependence on its uncompressed length (L_0, which is an integer number N_z of repetitions in the longitudinal direction of the basic structure shown in Figure 1). Hence, we focus our attention on the NTs with the lowest strain energy radius reported,[34,37,59] namely N_θ = 10. The general procedure is as follows: first we generate an imogolite of a given initial length 10 < L_0 < 100 nm, then we relax the structure using a combination of the FIRE method[60] and conjugate gradient (including box optimization). We combine both methods since in the LAMMPS code (at least for the present time) the box optimization is not yet implemented with the FIRE method, but it is possible with conjugate gradient. On the other hand, the FIRE method is able to find configurations of lower energy than a simple conjugate gradient. Once the relaxation stage is finished, we begin the MD simulations with a time-step of 1 fs, constraining the OH bonds with the SHAKE algorithm,[61] and imposing an initial random velocity for the atoms taken from a 3D Gaussian velocity distribution at 10 K. Then the imogolite is maintained at zero pressure for 10 ps using an isenthalpic ensemble (NPH) combined with a rescaling of velocities to keep the temperature around 10 K. After that, we change to a constant volume ensemble (NVE) integration combined with the rescaling of velocities for other 10 ps. Finally, we start the compression test, applying a constant engineering strain rate α along the axis of the NT (periodic) by reducing the longitudinal length of the computation box, following the expression:

$$L(t) = L_0(1 - \alpha t) \quad (2)$$

where L_0 is the initial length of the NT along its axis, $L(t)$ is the time dependent length, and $t = n\Delta t$ is the time with a time-step Δt = 1 fs, in all of the cases. We can define the strain for the NT as

$$\epsilon = \frac{L_0 - L}{L_0} \quad (3)$$

and we use $\alpha = 10^8$ s^{-1} in all our simulations. Simulations with slower strain rates give rise to similar results. In Figure S4 (Supporting Information), we plot the stress vs strain for L_0 = 10 nm where we compare the case of $\alpha = 10^8$ s^{-1} with $\alpha = 10^7$ s^{-1}.

DOI: 10.1021/acs.jpcc.6b04564
J. Phys. Chem. C 2016, 120, 14428−14434

RESULTS

To illustrate the general procedure and our results, first we are going to describe in detail the particular case of L_0 = 40 nm compression. Some lateral views during the compression of the imogolite NT is shown in Figure 2a for ϵ 0.05, 0.1, and 0.15 as

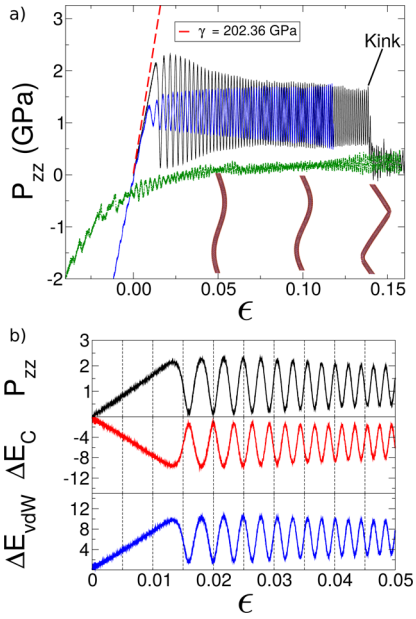

Figure 2. (a) P_{zz} (stress) vs strain curve for a 40 nm imogolite NT. The black line corresponds to the compression, while the blue (green) line corresponds to an elongation of a stressed situation of the imogolite, beginning just before (after) the occurrence of the kink in the NT wall (ϵ = 0.14). The same Young modulus ≈200 GPa is calculated for the compression and elongation process, which is in good agreement with previously published results.[28,44−46] (b) Detailed behavior of pressure and the change in energy with respect to zero strain during the first stage of the compression process. Stress in GPa, change in Coulomb energy ΔE_C, and change in van der Waals energy ΔE_{vdW} in meV per atom. As can be seen, coiling process could be explained because the Coulombian forces and the van der Waals forces are out of phase. In this sense, when starting from zero strain the Coulomb energy increases while the van der Waals energy decreases.

insets. In addition, we include more insets with lateral and axial views of these process in Figure S1 (Supporting Information). We can observe how the NT begins to coil around its original central axis, in such a way that its projection in the *xy* plane (axial projection) begins to take the shape of an ellipse. In this case, the coiling mechanism is present until a kink appears in the wall of the NT at around ϵ > 0.14. Latter in this manuscript we are going to quantify this behavior with an estimation of the curvature along the *z* axis during the compression of the NT.

In Figure 2a, we plot the stress vs strain curve for the same case just mentioned. The stress is estimated as the pressure along the NT axis and it is calculated from the stress tensor and the direct evaluation of the virial.[62] In the calculation the effective volume of the NT is estimated with the surface mesh tool included in the OVITO program.[57,58] Briefly, our estimation of the volume is based on a geometric criterion. The method uses a probe sphere with a radius similar to the nearest neighbor distance. In this case, we use a sphere of radius 0.3 nm, such that it does not fit between inner or outer hydroxyls. OVITO provides the solid volume fraction of the sample, and finally we calculate the NT volume multiplying the total volume of the box by this fraction. As usual in these kinds of tests, we observe a linear behavior for small strain i.e., for $\epsilon \lesssim$ 0.01. In Figure 2a the segmented red line corresponds to a linear regression for the stress in this linear regime. The slope of this line is about $\gamma \sim$ 200 GPa which corresponds, roughly, to the Young modulus of the NT near the zero strain condition. This value is in good agreement with previous theoretical results, which predict values between 122 and 479 GPa.[28,38,44−46] From all of the reported theoretical results, those from Teobaldi et al.[44] are the only DFT calculations reported, and as they mentioned, the GGA framework is known to underestimate the elastic constant of extended metal-oxide structures, so their results represents a lower limit for what could be expected in the laboratory. In this sense, the 200 GPa we calculated seem to be a reasonable estimate, compared to the range of 122−168 GPa reported in the DFT work. In addition, although CLAYFF was not parametrized explicitly with respect to mechanical properties, this potential has been extensively used in studies of mechanical properties of clays with good agreement with DFT and experiments.[63−66]

For $\epsilon \sim$ 0.015 the stress reaches a maximum of 2.13 GPa and an oscillating regime begins, that coincides with the coiling of the NT until the first kinks appear for $\epsilon \approx$ 0.14, which coincides with a sharp stress drop. This phase is still almost reversible, as can be seen in Figure 2a, where we also plot a continuous blue line that represents an elongation process that begins with a configuration with a strain in a point just before the kink occurrence at $\epsilon \approx$ 0.14 using the same value α, but negative, as the one used for the compression. We observe a similar oscillating stress behavior for $\epsilon \gtrsim$ 0.015, and a similar Young modulus of $\gamma \approx$ 200 GPa for small strain. In the same way, the green line shows the elongation process after the kink occurrence, showing that this rupture process is an irreversible damage. In conclusion, the coiling of imogolite during the compression is a mechanism that avoids the rupture of the NT and allows its elastic behavior under successive compression and elongation.

To explain the origin of the coiling mechanism we plot in Figure 2b the variation of Coulomb (ΔE_C) and van der Waals (ΔE_{vdW}) energies as a function of strain, with respect to zero strain. At the beginning of the compression the Coulomb energy is linearly reduced, while the van der Waals energy increases. Although the magnitude of the Coulomb energy is much larger than the van der Waals contribution, during the coiling regime these energies seem to compensate each other almost exactly, in an oscillatory manner, to produce the oscillating stress. Hence, the coiling could be explained basically by a competition of both forces.

In a perfect imogolite NT, each aluminum atom is bonded to six oxygen atoms forming an octahedral shape. We observe that when some of the aluminum atoms reduce their coordination, the kink appears. In Figure 3 we show the kink generation process of the L_0 = 40 nm at $\approx\epsilon \sim$ 0.14. To facilitate the visualization, we only draw the aluminum atoms, and we colored them considering the number of oxygen atoms inside a cutoff distance less than 2.3 Å. We chose this cutoff considering that the optimal bond distance of Al−O is about 1.95 Å and there are no other oxygen atoms before 3.2 Å in the NT structure. In this way, blue atoms have six oxygens inside the cutoff, green for the case of five oxygen atoms, and red corresponds to aluminum with four or less neighboring oxygen atoms. In Figure 3a we show the case just before the kink, with a NT that looks perfect, with every aluminum atom well

DOI: 10.1021/acs.jpcc.6b04564
J. Phys. Chem. C 2016, 120, 14428−14434

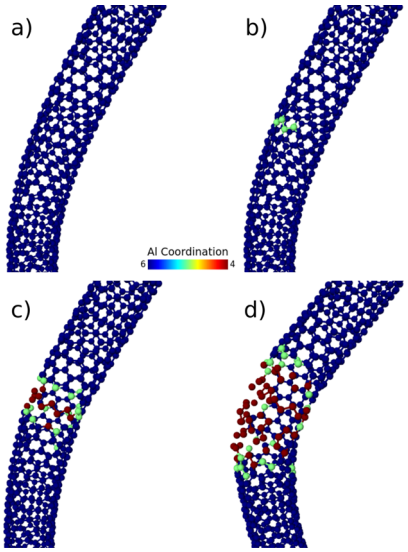

Figure 3. Kink occurrence as illustrated by the aluminum atomic coordination, which refers to the number of oxygen atom inside a sphere of radius 2.3 Å of around each aluminum atom. To facilitate the visualization, only the Al atoms were drawn, and the bonds are included only when the Al−Al distance is <3.2 Å. This sequence of snapshots takes place in around 20 fs.

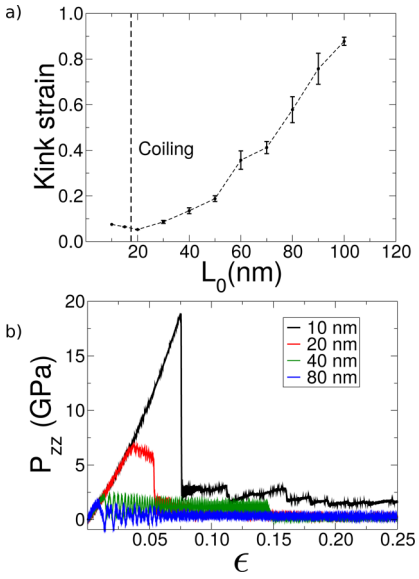

Figure 4. (a) Mean strain for the first kink occurrence, with error bars (mean deviation). In the L_0 < 20 nm cases, we do not observe coiling of the NTs before rupture, but the bucking of the NT does occur. (b) Curves of stress vs strain for L_0 = 10, 20, 40, and 80 nm. As can be seen the strain value for the beginning of the coiling is inversely proportional to L_0, and for L_0 < 20 nm the stress of the system is quite large before the coiling can happen and inevitably the NT collapses.

coordinated. For a slightly larger strain, namely 2 fs after the first snapshot, in Figure 3b we observe four undercoordinated aluminum atoms with only five oxygen neighboring atoms. Then in Figure 3c, 4 fs forward in time, aluminum atoms with even smaller coordination do appear. Finally, 20 fs after the first snapshot, in Figure 3d, the kink is formed. At this point the failure is irreversible, which means that if we try to elongate the NT from this point on we are not able to recover a NT that is similar to the original uncompressed structure, with all the aluminum atoms well coordinated, as we discussed above. Hence, the kink occurrence is due to the nucleation of aluminum atoms with reduced coordination, forming a ridge that quickly covers the whole cross section of the NT.

In addition to the L_0 = 40 nm case, in Figure 4a we show a summary picture of all the simulations for NTs ranging from 10 to 100 nm. In this plot, we compare the strain value for which the kink appears, with respect to the uncompressed length of the imogolite NT. For each length, we carried out 11 independent calculations starting with different initial velocities distributions. In the plot we show the mean value and the standard deviation for each length as error bars. For L_0 < 20 nm, there is no coiling stage before the rupture of the NT; e.g., the coiling stage does not appear in the stress vs strain curve. In this particular case, we observe the rupture of the NT due to the bucking process. On the other hand, we observe that the NTs of larger uncompressed length break for an increasingly larger strain. Also, it becomes clear that for uncompressed lengths larger than 100 nm the NT are able to coil without kinking even as we approach the fully compressed case $\epsilon \sim 1$. Moreover, for five calculations of L_0 = 100 nm, we do not observe any kinking process when reaching a strain up to ϵ = 0.95. We will see below that this NT is not able to reach the necessary curvature for breaking. From a practical point of view we can ensure imogolite always tends to coil under compression, and lengths <20 nm only are observed during the first stages of the aging of imogolite, with very small amounts present.[5,41] On the other hand, there are recent reports of synthesis of imogolite and Ge−imogolite with lengths up to 700 nm.[42,67] Finally, in Figure 4b, we show curves of stress vs strain for L_0 = 10, 20, 40, and 80 nm. As can be seen, the strain value for the beginning of coiling to occur is inversely proportional to L_0, and for L_0 < 20 nm, the stress of the system is quite large before the coiling can happen and inevitably the NT collapses. We can also note that the Young modulus, estimated by the slope of P_{zz} vs strain ϵ in Figure 4b, is about 200 GPa for a range of uncompressed lengths L_0. Although our estimations of the Young Modulus agree reasonably well with other values reported in the literature, it is true that for the conditions we consider here it would be of interest to use a molecular dynamical method that consider more explicitly the quantum mechanical properties close to the situation when the kinking occurs, such as reactive force fields,[68] or directly with DFT or SCC-DFTB methods.[28] However, since the shortest NT where we observed the coiling mechanism is 20 nm, which includes 6720 atoms, a DFT calculation would require extremely large computational resources.

From the discussion above, we realize that the radius of curvature may be a useful characterization of the nonlinear behavior of the compression process, especially to characterize the transition from coiling to kinking. To properly parametrize a curve from which we can compute an effective radius of curvature, we consider the center of mass position of each set of N_θ silicon atoms that form the angular structure, that repeats N_z times to form the longitudinal NT of uncompressed length L_0. In Figure 1c we show the silicon rings. In this way we obtain the position $\mathbf{r}_k = [x_k, y_k, z_k]$ of N_z points (k = 1, ..., N_z) along the NT. Notice that the coordinate system is chosen such that x and y correspond to transverse directions, and z to the longitudinal direction along the NT. Since we assume periodic boundary conditions (with an initial relaxed box length), we repeat this structure in the negative and positive longitudinal

DOI: 10.1021/acs.jpcc.6b04564
J. Phys. Chem. C 2016, 120, 14428−14434

direction of the uncompressed NT, so that we can avoid boundary effects when we compute a cubic spline for each of the 3 coordinates of the center of mass. The cubic spline is parametrized by λ, such that $\mathbf{r}(\lambda = k) = [x_n, y_n, z_n]$, and it allows to have 2 continuous (space varying) derivatives.

The curvature of a three-dimensional curve, parametrized by λ in three-dimensional Cartesian space, is defined as

$$\kappa(\lambda) = \frac{|\dot{r} \times \ddot{r}|}{|\dot{r}|^3}$$

where the derivatives are taken with respect to the λ. The radius of curvature is then defined by

$$R(\lambda) = \frac{1}{\kappa}$$

A dynamical view of the generation process is illustrated in Figure 5, where we observe how R at the position of the kink

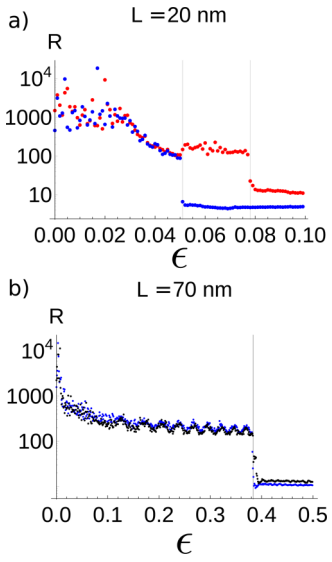

Figure 5. Value of R at the position where the kinking occurs (2 kinks occur, but at different times) as a function of the strain. (a) We show the L_0 = 20 nm case and (b) L_0 = 70 nm.

evolves as we compress the NT. Notice that in the case analyzed for L_0 = 20 nm there are two kinks that form at different times (or strains), and we follow both in time. For both kinks the transition is quite violent. We also notice that during the coiling process (before the vertical line that denotes the kink transition) the NT adjusts to the strain increase by a coiling that reduces R, but which eventually reaches a critical value $R_c(L_0)$ at which the NT can only kink to adjust the strain increase, i.e., coiling is not able to account for the increase in strain. It is interesting to notice that after the first kink forms the radius of curvature of the system, far away from the kink, relaxes somewhat (see red curve for the second kink), until the next kink appears. It is interesting to observe that the critical value of the radius of curvature at which both kinks occur are similar. In Figure 5b we show the dynamical behavior of the curvature at the position of the kink for L_0 = 70 nm. In this case we have two kinks that form at about the same time. During the evolution we clearly see how the coiling is able to adapt to the increased strain by reducing the radius of curvature (i.e., by coiling), until it reaches a critical value, very similar to the one obtained for the uncompressed length L_0 = 20 nm, and kinks. This critical value is similar for both kinks. For other uncompressed lengths L_0 the system can form more than two kinks, but the critical value of the curvature, where the kinking occurs, seems to be universal for the different L_0 values. It is important to mention that for very large L_0 the system can compensate with coiling, without kinking, even for an ϵ value close to one.

CONCLUSIONS

In this contribution, we have studied the mechanical properties of an imogolite NT under a compression strain, for different uncompressed lengths of the NT. We have found an initial linear regime in which a Young modulus can be computed. For L_0 > 20 nm the compressed NT resolve the strain increase by a coiling phase. This phase adapts to the decrease in strain by decreasing the radius of curvature, until it reaches a critical value $R_c \approx$ 100 nm, which seems to be reasonably universal, at which point the NT kinks. We notice that it is common for the NT to relax the stresses by means of more than one kink. The kinking is a violent process through which the NT changes the coiling process to adapt to the strain increase. Also, it is important to mention that imogolite nanotubes can be synthesized with length that can reach values up to 500 nm.[41,42,67] Our values of the Young modulus are similar to the values calculated for DFT for much shorter nanotubes.[44] Here new mechanisms are uncovered under dynamic loading, and much longer nanotubes were studied. Given the difficulty of measuring mechanical properties of nanotubes in the laboratory, computational studies can offer useful insights into plastic yielding and failure of nanotubes. Finally, it is important to remark that these predictions are for a perfect and dry nanotubes. The behavior could be different from what can be observed under laboratory conditions, as imogolite is synthesized immersed in water. Similarly, depending on the synthesis conditions, defects in the wall of nanotubes are expected.[69] The case of a NT in the presence of water or with defects will be studied in a future manuscript.

ASSOCIATED CONTENT

Supporting Information

The Supporting Information is available free of charge on the ACS Publications website at DOI: 10.1021/acs.jpcc.6b04564.

Insets with lateral and axial views of compression process for L_0 = 40 nm, time evolution of center of mass of Si rings (projected in the xy plane) and the radius of curvature along z position for L_0 = 20 nm and L_0 = 70 nm, and stress vs strain curves for L_0 = 10 nm for different engineering strain rates (PDF)

AUTHOR INFORMATION

Corresponding Authors

*(R.I.G.) E-mail: rafaelgonzalezvaldes@gmail.com.
*(J.A.V.) E-mail: alejo@macul.ciencias.uchile.cl.

Notes

The authors declare no competing financial interest.

ACKNOWLEDGMENTS

We thank to Prof. Miguel Kiwi for valuable discussions and his constant support. This work was supported by the Fondo Nacional de Investigaciones Científicas y Tecnológicas (FONDECYT, Chile) under Grant No. 3140526 (R.I.G.), No. 1150718 (J.A.V.), and Nos. 1160639 and 1130272 (J.R.),

DOI: 10.1021/acs.jpcc.6b04564
J. Phys. Chem. C 2016, 120, 14428−14434

by Financiamiento Basal para Centros Científicos y Tecnológicos de Excelencia (J.R., J.A.V., and R.I.G.), and by Anillo CONICYT PIA ACT-1405 (J.A.V. and J.R.). E.M.B. expresses thanks for support from SeCTyP-UNCuyo under Grant No. M003, and ANPCyT under Grant No. PICT-2014-0696.

REFERENCES

(1) Iijima, S. Helical Microtubules of Graphitic Carbon. *Nature* **1991**, *354*, 56−58.
(2) Tenne, R.; Margulis, L.; Genut, M.; Hodes, G. Polyhedral and Cylindrical Structures of Tungsten Disulphide. *Nature* **1992**, *360*, 444−446.
(3) Remskar, M. Inorganic Nanotubes. *Adv. Mater.* **2004**, *16*, 1497−1504.
(4) Yoshinaga, N.; Aomine, A. Imogolite in Some Ando Soils. *Soil Sci. Plant Nutr.* **1962**, *8*, 22−29.
(5) Yucelen, G. I.; Kang, D.; Guerrero-Ferreira, R.; Wright, E.; Beckham, H. W.; Nair, S. Shaping Single-Walled Metal Oxide Nanotubes from Precursors of Controlled Curvature. *Nano Lett.* **2012**, *12*, 827−832.
(6) Gustafsson, J. P. The Surface Chemistry of Imogolite. *Clays Clay Miner.* **2001**, *49*, 73−80.
(7) Arancibia-Miranda, N.; Escudey, M.; Pizarro, C.; Denardin, J. C.; García-González, M. T.; Fabris, J. D.; Charlet, L. Preparation and Characterization of a Single-Walled Aluminosilicate Nanotube-Iron Oxide Composite: Its Applications to Removal of Aqueous Arsenate. *Mater. Res. Bull.* **2014**, *51*, 145−152.
(8) Veerabadran, N.; Price, R.; Lvov, Y. Clay Nanotubes for Encapsulation and Sustained Release of Drugs. *Nano* **2007**, *02*, 115−120.
(9) Park, S.; Lee, Y.; Kim, B.; Lee, J.; Jeong, Y.; Noh, J.; Takahara, A.; Sohn, D. Two-Dimensional Alignment of Imogolite on a Solid Surface. *Chem. Commun.* **2007**, *28*, 2917−2919.
(10) Marzan, L. L.; Philipse, A. Synthesis of Platinum Nanoparticles in Aqueous Host Dispersions of Inorganic (Imogolite) Rods. *Colloids Surf., A* **1994**, *90*, 95−109.
(11) Imamura, S.; Hayashi, Y.; Kajiwara, K.; Hoshino, H.; Kaito, C. Imogolite: A Possible New Type of Shape-Selective Catalyst. *Ind. Eng. Chem. Res.* **1993**, *32*, 600−603.
(12) Imamura, S.; Kokubu, T.; Yamashita, T.; Okamoto, Y.; Kajiwara, K.; Kanai, H. Shape-Selective Copper-Loaded Imogolite Catalyst. *J. Catal.* **1996**, *160*, 137−139.
(13) Arancibia-Miranda, N.; Silva-Yumi, J.; Escudey, M. Effect of Cations in the Background Electrolyte on the Adsorption Kinetics of Copper and Cadmium and the Isoelectric Point of Imogolite. *J. Hazard. Mater.* **2015**, *299*, 675−684.
(14) Denaix, L.; Lamy, Y.; Bottero, J. Y. Structure and Affinity Towards Cd^{2+}, Cu^{2+}, Pb^{2+} of Synthetic Colloidal Amorphous Aluminosilicates and their Precursors. *Colloids Surf., A* **1999**, *158*, 315−325.
(15) Wilson, M. A.; Lee, G. S. H.; Taylor, R. C. Benzene Displacement on Imogolite. *Clays Clay Miner.* **2002**, *50*, 348−351.
(16) Zanzottera, C.; Armandi, M.; Esposito, S.; Garrone, E.; Bonelli, B. CO_2 Adsorption on Aluminosilicate Single-Walled Nanotubes of Imogolite Type. *J. Phys. Chem. C* **2012**, *116*, 20417−20425.
(17) Kang, D.; Zang, J.; Jones, C.; Nair, S. Single-Walled Aluminosilicate Nanotube/Poly(Vinyl Alcohol) Nanocomposite Membranes. *ACS Appl. Mater. Interfaces* **2012**, *4*, 965−976.
(18) Kang, D.-Y.; Brunelli, N. A.; Yucelen, G. I.; Venkatasubramanian, A.; Leisen, J.; Hesketh, P. J.; Jones, C. W.; Nair, S.; Zang, J. Direct Synthesis of Single-Walled Aminoaluminosilicate Nanotubes with Enhanced Molecular Adsorption Selectivity. *Nat. Commun.* **2014**, *5*, 3342.
(19) Kuc, A.; Heine, T. Shielding Nanowires and Nanotubes with Imogolite: A Route to Nanocables. *Adv. Mater.* **2009**, *21*, 4353−4356.
(20) Yamamoto, K.; Otsuka, H.; Takahara, A. Preparation of Novel Polymer Hybrids from Imogolite Nanofiber. *Polym. J.* **2007**, *39*, 1−15.
(21) Yah, W.; Irie, A.; Jiravanichanun, N.; Otsuka, H.; Takahara, A. Molecular Aggregation State and Electrical Properties of Terthiophenes/Imogolite Nanohybrids. *Bull. Chem. Soc. Jpn.* **2011**, *84*, 893−902.
(22) Ma, W.; Yah, W.; Otsuka, H.; Takahara, A. Application of Imogolite Clay Nanotubes in Organic-Inorganic Nanohybrid Materials. *J. Mater. Chem.* **2012**, *22*, 11887−11892.
(23) Geraldo, D.; Arancibia-Miranda, N.; Villagra, N.; Mora, G.; Arratia-Perez, R. Synthesis of CdTe QDs/Single-Walled Aluminosilicate Nanotubes Hybrid Compound and Their Antimicrobial Activity on Bacteria. *J. Nanopart. Res.* **2012**, *14*, 1−9.
(24) Thomas, B.; Coradin, T.; Laurent, G.; Valentin, R.; Mouloungui, Z.; Babonneau, F.; Baccile, N. Biosurfactant-Mediated One-Step Synthesis of Hydrophobic Functional Imogolite Nanotubes. *RSC Adv.* **2012**, *2*, 426−435.
(25) Kang, D.; Zang, J.; Jones, C.; Nair, S. Single-Walled Aluminosilicate Nanotubes with Organic-Modified Interiors. *J. Phys. Chem. C* **2011**, *115*, 7676−7685.
(26) Bottero, I.; Bonelli, B.; Ashbrook, S. E.; Wright, P. A.; Zhou, W.; Tagliabue, M.; Armandi, M.; Garrone, E. Synthesis and Characterization of Hybrid Organic/Inorganic Nanotubes of the Imogolite Type and Their Behaviour Towards Methane Adsorption. *Phys. Chem. Chem. Phys.* **2011**, *13*, 744−750.
(27) Ramírez, M.; González, R. I.; Munoz, F.; Valdivia, J. A.; Rogan, J.; Kiwi, M. Coaxial Nanocable Composed by Imogolite and Carbon Nanotubes. *AIP Conf. Proc.* **2015**, *1702*, 050005.
(28) Guimarães, L.; Enyashin, A. N.; Frenzel, J.; Heine, T.; Duarte, H. A.; Seifert, G. Imogolite Nanotubes: Stability, Electronic, and Mechanical Properties. *ACS Nano* **2007**, *1*, 362−368.
(29) Farmer, V. C.; Fraser, A. R.; Tait, J. M. Synthesis of Imogolite: A Tubular Aluminium Silicate Polymer. *J. Chem. Soc., Chem. Commun.* **1977**, 462−463.
(30) Mukherjee, S.; Bartlow, V. M.; Nair, S. Phenomenology of the Growth of Single-Walled Aluminosilicate and Aluminogermanate Nanotubes of Precise Dimensions. *Chem. Mater.* **2005**, *17*, 4900−4909.
(31) Levard, C.; Masion, A.; Rose, J.; Doelsch, E.; Borschneck, D.; Dominici, C.; Ziarelli, F.; Bottero, J. Y. Synthesis of Imogolite Fibers from Decimolar Concentration at Low Temperature and Ambient Pressure: A Promising Route for Inexpensive Nanotubes. *J. Am. Chem. Soc.* **2009**, *131*, 17080−17081.
(32) Arancibia-Miranda, N.; Escudey, M.; Molina, M.; García-González, M. Use of Isoelectric Point and pH to Evaluate the Synthesis of a Nanotubular Aluminosilicate. *J. Non-Cryst. Solids* **2011**, *357*, 1750.
(33) Arancibia-Miranda, N.; Escudey, M.; Molina, M.; García-González, M. Kinetic and Surface Study of Single-Walled Aluminosilicate Nanotubes and Their Precursors. *Nanomaterials* **2013**, *3*, 126−140.
(34) González, R. I.; Ramírez, R.; Rogan, J.; Valdivia, J. A.; Munoz, F.; Valencia, F.; Ramírez, M.; Kiwi, M. Model for Self-Rolling of an Aluminosilicate Sheet into a Single-Walled Imogolite Nanotube. *J. Phys. Chem. C* **2014**, *118*, 28227−28233.
(35) González, R. I.; Ramírez, R.; Rogan, J.; Valdivia, J. A.; Munoz, F.; Valencia, F.; Ramírez, M.; Kiwi, M. Self-Rolling of an Aluminosilicate Sheet Into a Single Walled Imogolite Nanotube: The Role of the Hydroxyl Arrangement. *AIP Conf. Proc.* **2015**, *1702*, 050004.
(36) Konduri, S.; Mukherjee, S.; Nair, S. Controlling Nanotube Dimensions: Correlation between Composition, Diameter, and Internal Energy of Single- Walled Mixed Oxide Nanotubes. *ACS Nano* **2007**, *1*, 393−402.
(37) Alvarez-Ramírez, F. Ab Initio Simulation of the Structural and Electronic Properties of Aluminosilicate and Aluminogermanate Natotubes with Imogolite-Like Structure. *Phys. Rev. B: Condens. Matter Mater. Phys.* **2007**, *76*, 125421.
(38) Lourenco, M. P.; Guimarães, L.; da Silva, M. C.; de Oliveira, C.; Heine, T.; Duarte, H. A. Nanotubes with Well-Defined Structure: Single- and Double-Walled Imogolites. *J. Phys. Chem. C* **2014**, *118*, 5945−5953.

DOI: 10.1021/acs.jpcc.6b04564
J. Phys. Chem. C 2016, 120, 14428−14434

(39) Demichelis, R.; Noel, Y.; D'Arco, P.; Maschio, L.; Orlando, R.; Dovesi, R. Structure and Energetics of Imogolite: A Quantum Mechanical ab Initio Study with B3LYP Hybrid Functional. *J. Mater. Chem.* **2010**, *20*, 10417−10425.
(40) Cradwick, P. D. G.; Farmer, V. C.; Russell, J. D.; Masson, C. R.; Wada, K.; Yoshinaga, N. Imogolite, a Hydrated Aluminium Silicate of Tubular Structure. *Nature, Phys. Sci.* **1972**, *240*, 187−189.
(41) Yucelen, G. I.; Kang, D.; Schmidt-Krey, I.; Beckham, H. W.; Nair, S. A Generalized Kinetic Model for the Formation and Growth of Single-Walled Metal Oxide Nanotubes. *Chem. Eng. Sci.* **2013**, *90*, 200.
(42) Paineau, E.; Krapf, M.-E. M.; Amara, M.-S.; Matskova, N. V.; Dozov, I.; Rouzière, S.; Thill, A.; Launois, P.; Davidson, P. A Liquid-Crystalline Hexagonal Columnar Phase in Highly-Dilute Suspensions of Imogolite Nanotubes. *Nat. Commun.* **2016**, *7*, 10271.
(43) Bonelli, B.; Bottero, I.; Ballarini, N.; Passeri, S.; Cavani, F.; Garrone, E. IR Spectroscopic and Catalytic Characterization of the Acidity of Imogolite-Based Systems. *J. Catal.* **2009**, *264*, 15−30.
(44) Teobaldi, G.; Beglitis, N. S.; Fisher, A. J.; Zerbetto, F.; Hofer, W. A. Hydroxyl Vacancies in Single-Walled Aluminosilicate and Aluminogermanate Nanotubes. *J. Phys.: Condens. Matter* **2009**, *21*, 195301.
(45) Liou, K.-H.; Tsou, N.-T.; Kang, D.-Y. Relationships Among the Structural Topology, Bond Strength, and Mechanical Properties of Single-Walled Aluminosilicate Nanotubes. *Nanoscale* **2015**, *7*, 16222−16229.
(46) Liou, K.-H.; Kang, D.-Y. Defective Single-Walled Aluminosilicate Nanotubes: Structural Stability and Mechanical Properties. *ChemNanoMat* **2016**, *2*, 189−195.
(47) Plimpton, S. J. Fast Parallel Algorithms for Short-Range Molecular Dynamics. *J. Comput. Phys.* **1995**, *117*, 1−19.
(48) Brown, W. M.; Wang, P.; Plimpton, S. J.; Tharrington, A. N. Implementing Molecular Dynamics on Hybrid High Performance Computers - Short Range Forces. *Comput. Phys. Commun.* **2011**, *182*, 898−911.
(49) Brown, W. M.; Kohlmeyer, A.; Plimpton, S. J.; Tharrington, A. N. Implementing Molecular Dynamics on Hybrid High Performance Computers - Particle-Particle Particle-Mesh. *Comput. Phys. Commun.* **2012**, *183*, 449−459.
(50) Brown, W. M.; Yamada, m. Implementing Molecular Dynamics on Hybrid High Performance Computers - Three-Body Potentials. *Comput. Phys. Commun.* **2013**, *184*, 2785−2793.
(51) Cygan, R. T.; Liang, J. J.; Kalinichev, A. G. Molecular Models of Hydroxide, Oxyhydroxide, and Clay Phases and the Development of a General Force Field. *J. Phys. Chem. B* **2004**, *108*, 1255−1266.
(52) Konduri, S.; Mukherjee, S.; Nair, S. Strain Energy Minimum and Vibrational Properties of Single-Walled Aluminosilicate Nanotubes. *Phys. Rev. B: Condens. Matter Mater. Phys.* **2006**, *74*, 33401.
(53) Konduri, S.; Tong, H. M.; Chempath, S.; Nair, S. Water in Single-Walled Aluminosilicate Nanotubes: Diffusion and Adsorption Properties. *J. Phys. Chem. C* **2008**, *112*, 15367−15374.
(54) Zang, J.; Konduri, S.; Nair, S.; Sholl, D. Self-Diffusion of Water and Simple Alcohols in Single-Walled Aluminosilicate Nanotubes. *ACS Nano* **2009**, *3*, 1548−1556.
(55) Zang, J.; Chempath, S.; Konduri, S.; Nair, S.; Sholl, D. S. Flexibility of Ordered Surface Hydroxyls Influences the Adsorption of Molecules in Single-Walled Aluminosilicate Nanotubes. *J. Phys. Chem. Lett.* **2010**, *1*, 1235−1240.
(56) Ewald, P. P. Die Berechnung Optischer und Elektrostatischer Gitterpotentiale. *Ann. Phys.* **1921**, *369*, 253−287.
(57) Stukowski, A. Visualization and Analysis of Atomistic Simulation Data With OVITO-the Open Visualization Tool. *Modell. Simul. Mater. Sci. Eng.* **2010**, *18*, 015012.
(58) Stukowski, A. Computational Analysis Methods in Atomistic Modeling of Crystals. *JOM* **2014**, *66*, 399−407.
(59) Poli, E.; Elliott, J. D.; Hine, N. D. M.; Mostofi, A. A.; Teobaldi, G. Large-Scale Density Functional Theory Simulation of Inorganic Nanotubes: a Case Study on Imogolite Nanotubes. *Mater. Res. Innovations* **2015**, *19*, S272−S282.
(60) Bitzek, E.; Koskinen, P.; Gähler, F.; Moseler, M.; Gumbsch, P. Structural Relaxation Made Simple. *Phys. Rev. Lett.* **2006**, *97*, 170201.
(61) Ryckaert, J.-P.; Ciccotti, G.; Berendsen, H. J. Numerical Integration of the Cartesian Equations of Motion of a System With Constraints: Molecular Dynamics of N-Alkanes. *J. Comput. Phys.* **1977**, *23*, 327−341.
(62) Thompson, A. P.; Plimpton, S. J.; Mattson, W. General Formulation of Pressure and Stress Tensor for Arbitrary Many-Body Interaction Potentials Under Periodic Boundary Conditions. *J. Chem. Phys.* **2009**, *131*, 154107.
(63) Suter, J. L.; Coveney, P. V.; Greenwell, H. C.; Thyveetil, M.-A. Large-Scale Molecular Dynamics Study of Montmorillonite Clay: Emergence of Undulatory Fluctuations and Determination of Material Properties. *J. Phys. Chem. C* **2007**, *111*, 8248−8259.
(64) Suter, J. L.; Coveney, P. V. Computer Simulation Study of the Materials Properties of Intercalated and Exfoliated Poly (Ethylene) Glycol Clay Nanocomposites. *Soft Matter* **2009**, *5*, 2239−2251.
(65) Kalra, A.; Parks, D. M.; Rutledge, G. C. Molecular Simulation of Strain Dependence of Vibrational Frequencies for Montmorillonite Clay and Analysis of Strain Transfer in a Polymer-Clay Nanocomposite. *Macromolecules* **2007**, *40*, 140−144.
(66) Teich-McGoldrick, S. L.; Greathouse, J. A.; Cygan, R. T. Molecular Dynamics Simulations of Structural and Mechanical Properties of Muscovite: Pressure and Temperature Effects. *J. Phys. Chem. C* **2012**, *116*, 15099−15107.
(67) Amara, M.-S.; Paineau, E.; Bacia-Verloop, M.; Krapf, M.-E. M.; Davidson, P.; Belloni, L.; Levard, C.; Rose, J.; Launois, P.; Thill, A. Single-Step Formation of Micron Long (OH)3Al2O3Ge(OH) Imogolite-Like Nanotubes. *Chem. Commun.* **2013**, *49*, 11284−11286.
(68) van Duin, A. C. T.; Dasgupta, S.; Lorant, F.; Goddard, W. A. ReaxFF: A Reactive Force Field for Hydrocarbons. *J. Phys. Chem. A* **2001**, *105*, 9396−9409.
(69) Yucelen, G. I.; Choudhury, R. P.; Leisen, J.; Nair, S.; Beckham, H. W. Defect Structures in Aluminosilicate Single-Walled Nanotubes: A Solid-State Nuclear Magnetic Resonance Investigation. *J. Phys. Chem. C* **2012**, *116*, 17149−17157.

DOI: 10.1021/acs.jpcc.6b04564
J. Phys. Chem. C 2016, 120, 14428−14434